# Impact Analysis and Mitigation of Synchronization Dynamics for DQ Impedance Measurement

Hong Gong, *Student Member, IEEE*, Dongsheng Yang, *Member, IEEE*, and Xiongfei Wang, *Senior Member, IEEE*

***Abstract*—The small-signal stability assessment of three-phase systems can be performed using the measured impedances of the load and source. To obtain the dc steady-state operation point, the impedances are measured in the rotating *dq*-frame, and the phase angle is needed for the coordinate transformation used in both the perturbation injection and the impedance calculation. However, the phase estimation may introduce additional dynamics, affecting the accuracy of impedance measurements. This paper investigates the impact of synchronization dynamics on the accuracy of the measured impedance. It is revealed that the synchronization dynamic in the perturbation injection has little effect on the measured impedance, while the synchronization dynamic introduced in the impedance calculation can have significant effect. Based on the relationship between voltage and current in the measured *dq*-frame and in the actual *dq*-frame, an improved impedance calculation method is developed. The method can reduce the errors caused by the synchronization dynamics considering both the injected perturbations and system frequency variations. Finally, simulations and experimental results verify the accuracy of the theoretical analysis and the effectiveness of the method.**

***Index Terms*—Frequency domain analysis, impedance measurement, small-signal model, synchronization.**

## I. Introduction

As the proportion of power electronics devices in power systems keeps growing in recent years, the stability issues caused by converter-grid interactions have been increasingly reported [1]. To address these problems, the impedance-based stability analysis method has been widely applied to the power-electronics-based power systems [2], [3]. Yet, the analytical impedance model is difficult to be obtained in practice, since the system operators have no access to the control systems of converters. There is, thus, a growing demand for measuring the impedances of converters.

The dynamics of grid-connected power converters are time-varying and nonlinear when the phase-locked loop and the outer power control loops are considered [4]. In order to obtain the linearized impedance models of grid converters, the *dq*-transformation is usually used to transform the time-varying

Manuscript received July 10, 2018; revised September 30, 2018; accepted November 26, 2018. Date of publication December 10, 2018; date of current version June 10, 2019. Recommended for publication by Associate Editor L. Peng. *(Corresponding author: Dongsheng Yang.)*

The authors are with the Department of Energy Technology, Aalborg University, Aalborg 9220, Denmark (e-mail:

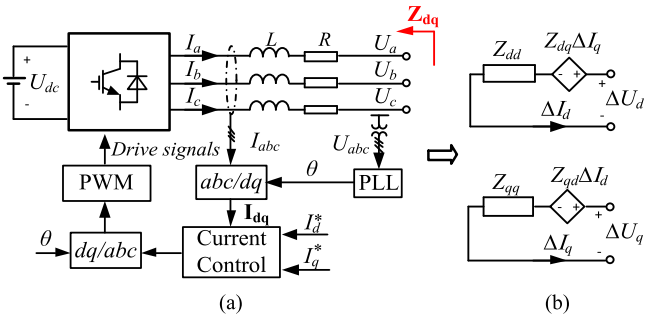


Fig. 1. (a) Three-phase voltage source converter. (b) The Small-signal model in the *dq*-frame.

set much lower than the lowest injected perturbation frequency to avoid the errors caused by synchronization dynamics [17], [18]. Yet, in this case, the control bandwidth of the PLL for the impedance calculation has to be set extremely low when the injected perturbation frequency is low, e.g., a few Hertz. A low-bandwidth PLL takes a long time to obtain the system frequency and may not accurately track the system frequency variations, affecting the accuracy of the impedance measurement.

In [15], the influence of PLL dynamics on the impedance measurement is analyzed and a correction method is developed. However, the impact of the frequency variation of ac system is not taken into account, and the impedance inaccuracies in some frequency points that are below the bandwidth of PLL used for impedance calculation still exist.

This paper, thus, presents a comprehensive analysis on the effect of synchronization dynamics on the *dq* impedance measurement. These effects may affect the accuracy of the impedance measurement. Then, to mitigate such effects, an improved impedance calculation method is developed. The accuracy of the analytical results and the effectiveness of the proposed method have been validated by the simulation and experiment results.

## II. Impedance Measurement in the DQ-Frame

### A. Small-Signal Impedance Model in the DQ-Frame

Fig. 1(a) shows an example of three-phase voltage source converter used to illustrate the concept of impedance model. $L$ and $R$ are filtered inductor and its parasitic resistor, respectively. $I_{abc}$ and $U_{abc}$ represent three-phase currents of converter and PCC voltages, respectively. $U_{\rm dc}$ is the dc voltage and $\theta$ denotes the synchronization phase generated by the PLL. For simplicity, only the current control and PLL are considered in this paper. $\mathbf{Z}_{\rm dq}$ is the *dq* impedance matrix of the converter, which models all circuit components, including physical components and control systems.

Fig. 1(b) shows the small-signal impedance model of the converter in the *dq*-frame. For the balanced and symmetrical three-phase ac system, the *dq* impedance model is widely used, since there exists a dc operating point in the *dq*-frame. Similar to dc systems, the relationship between the small variations of *dq*-axis voltages and currents are used to model the *dq* impedance characteristics of converters. Thus, the small-signal *dq* impedance model of converters can be derived by linearizing voltages and currents around its steady-state operating point as follows:

$$\begin{bmatrix}\Delta U_d\\ \Delta U_q\end{bmatrix} = \mathbf{Z_{dq}}\begin{bmatrix}\Delta I_d\\ \Delta I_q\end{bmatrix} = \begin{bmatrix}Z_{dd} & Z_{dq}\\ Z_{qd} & Z_{qq}\end{bmatrix}\begin{bmatrix}\Delta I_d\\ \Delta I_q\end{bmatrix} \quad (1)$$

where $\triangle$ denotes the small deviations of the respective variables from the equilibrium point.

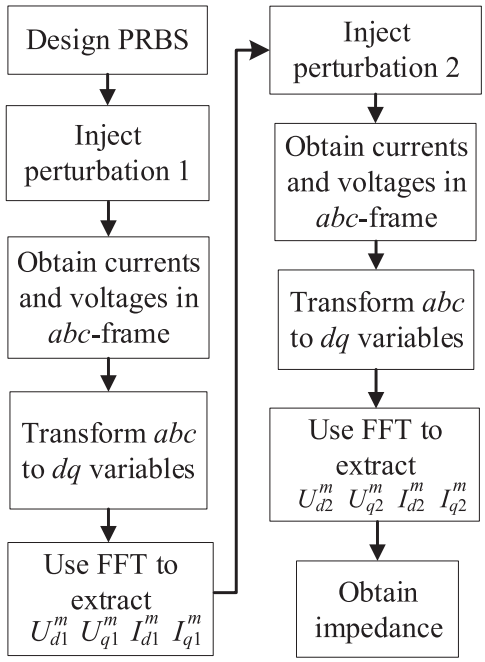


Fig. 2. Flowchart of the impedance measurement.

### B. Impedance Measurement Procedure and Algorithm

Fig. 2 illustrates the detailed flowchart of the impedance measurement procedure, which consists of designing of excitation signals, perturbation injection, data processing, and impedance calculation.

First, the excitation signals have to be chosen and designed. To facilitate the impedance measurement over a wide frequency range and save the measuring time, a broadband signal, i.e., the pseudo random binary sequence (PRBS) signal, is chosen as the excitation signal (perturbation). The magnitude and frequency of this excitation signal have to be appropriately designed to extract the converter dynamics [19]. On the one hand, the magnitude of the excitation signal has to be small to ensure that the system stays around its operating point. On the other hand, it has to be sufficiently large to reject noise disturbances. In general, the magnitude of the excitation signal is chosen between 5% and 10% of steady-state values [10], [11].

The next step is to inject the perturbation into the system to generate the voltage and current response of the converter. There are two types of perturbation injection methods: shunt current injection and series voltage injection. In this paper, the shunt current injection is used in the impedance measurement, since this method is easier to implement for the experimental verification. It is worth noting that the type of the injection method does not influence the impact analysis of the synchronization phase angle on the impedance measurement results [17].

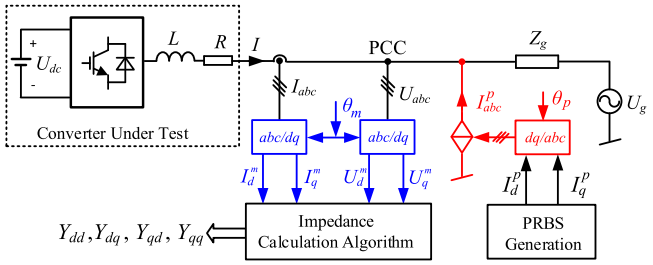


Fig. 3. System diagram of the impedance measurement setup.

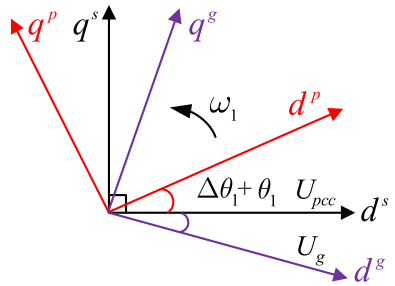


Fig. 4. Grid-, perturbation-, and PCC-voltage *dq*-frames.

Then, the measured output current and voltage of the converter are transformed to the rotating *dq*-frame. By applying the FFT to transformed variables, the magnitude, and phase information for each voltage and current at the injected frequency can be extracted at a time. To acquire the four entries of the impedance matrix as shown in (1), two linearly independent perturbations are applied.

Finally, based on the extracted magnitude and phase information, the impedance calculation algorithm developed in [15] was used to calculate the converter impedance in the *dq*-frame. Since in the small-signal analysis the converter acts as a current source, the impedance is interpreted as an admittance, which is given by

$$\begin{bmatrix} Y_{dd} & Y_{dq} \\ Y_{qd} & Y_{qq} \end{bmatrix} = \begin{bmatrix} I_{d1}^m & I_{d2}^m \\ I_{q1}^m & I_{q2}^m \end{bmatrix} \begin{bmatrix} U_{d1}^m & U_{d2}^m \\ U_{q1}^m & U_{q2}^m \end{bmatrix}^{-1} \tag{2}$$

where the subscripts "1" and "2" imply two linearly independent perturbations.

Fig. 3 shows the system diagram of the impedance measurement setup. To distinguish the influences of synchronization phase angles, two different synchronization phases $\theta_p$ and $\theta_m$ are used to denote the synchronization phase angles used for the perturbation injection and for the impedance calculation, respectively. Either the PLL or other alternative algorithms can be used to obtain the synchronization phase angles [20], [21]. In this setup, the PLL is adopted to generate the synchronization phase angle used for the perturbation injection and impedance calculation. It should be noted that the PLLs used for the perturbation injection and for the impedance calculation are different from the PLL used inside the converter under test. The PCC voltage is considered as the input of PLLs used for both the perturbation injection and the impedance calculation, and thus, the injected perturbations and system frequency variations affect the synchronization phase angle of the PLL. These influences are separated by two parts in respect to the purposes, i.e., the perturbation injection and the impedance calculation, which will be discussed in Section III and IV, respectively.

## III. Influence of Synchronization Dynamics on Perturbation Injection

The perturbation reference signal is first designed in the *dq*-frame and then transformed to *abc*-frame by using the inverse Park transformation, as shown in Fig. 3. When the synchronization phase angle $\theta_p$ used for the perturbation injection is different from the ideal PCC voltage phase $\theta_s$, the relationship between the voltage in the PCC-voltage *dq*-frame (superscript "*s*") and in the perturbation-voltage *dq*-frame (superscript "*p*") is written as

$$\begin{bmatrix} U_d^s \\ U_q^s \end{bmatrix} = \mathbf{T_{dq}}(\theta_p)\mathbf{T_{abc}}(\theta_s) \begin{bmatrix} U_d^p \\ U_q^p \end{bmatrix}. \tag{3}$$

$\mathbf{T}_{\mathrm{dq}}$ and $\mathbf{T}_{\mathrm{abc}}$ are *abc* to *dq* and *dq* to *abc* transformation matrices, respectively, which are defined as

$$\mathbf{T_{dq}}(\theta_p) = \sqrt{\frac{2}{3}} \begin{bmatrix} \cos(\theta_p) & \cos(\theta_p - 2\pi/3) & \cos(\theta_p + 2\pi/3) \\ -\sin(\theta_p) & -\sin(\theta_p - 2\pi/3) & -\sin(\theta_p + 2\pi/3) \end{bmatrix} \tag{4}$$

$$\mathbf{T_{abc}}(\theta_s) = \sqrt{\frac{2}{3}} \begin{bmatrix} \cos(\theta_s) & -\sin(\theta_s) \\ \cos(\theta_s - 2\pi/3) & -\sin(\theta_s - 2\pi/3) \\ \cos(\theta_s + 2\pi/3) & -\sin(\theta_s + 2\pi/3) \end{bmatrix}. \tag{5}$$

Fig. 4 shows the *dq*-frames aligned with the grid-, perturbation-, and PCC-voltage, respectively. Assuming that the synchronization phase angle used for the impedance calculation can be obtained accurately, it is aligned with the PCC-voltage *dq*-frame. $\triangle\theta_1+\theta_1$ denotes the angle difference between the perturbation-voltage *dq*-frame ($\theta_p$) and the PCC-voltage *dq*-frame ($\theta_s$), where $\triangle\theta_1$ is caused by the PLL used for the injected perturbation and $\theta_1$ is the initial phase of the perturbation-voltage *dq*-frame. The value of $\theta_1$ determines the proportion of the *d* and *q*-axis perturbation components injected into the system. Based on (3)–(5), the relationship between the voltage perturbation $U_{pd,q}^p$ in the perturbation-voltage *dq*-frame and in the PCC-voltage *dq*-frame is derived as

$$\begin{bmatrix} U_{pd0}^s + U_{pd}^s \\ U_{pq0}^s + U_{pq}^s \end{bmatrix} = \begin{bmatrix} \cos(\theta_1+\Delta\theta_1) & \sin(\theta_1+\Delta\theta_1) \\ -\sin(\theta_1+\Delta\theta_1) & \cos(\theta_1+\Delta\theta_1) \end{bmatrix} \begin{bmatrix} U_{pd0}^p + U_{pd}^p \\ U_{pq0}^p + U_{pq}^p \end{bmatrix} \tag{6}$$

where $U_{pd0,q0}^p$ and $U_{pd0,q0}^s$ represent the steady-state value of the perturbation in the perturbation-voltage *dq*-frame and in the PCC-voltage *dq*-frame, respectively.

Since $\triangle\theta_1$ is very small, the trigonometric functions can be approximated as $\sin\triangle\theta_1 \approx \triangle\theta_1$, $\cos\triangle\theta_1 \approx 1$. By eliminating the steady-state values, (6) can be further derived as

$$\begin{bmatrix} U_{pd}^s \\ U_{pq}^s \end{bmatrix} = \begin{bmatrix} \cos\theta_1 & \sin\theta_1 \\ -\sin\theta_1 & \cos\theta_1 \end{bmatrix} \begin{bmatrix} U_{pd}^p \\ U_{pq}^p \end{bmatrix} - \Delta\theta_1 \begin{bmatrix} \sin\theta_1 & -\cos\theta_1 \\ \cos\theta_1 & \sin\theta_1 \end{bmatrix} \begin{bmatrix} U_{pd0}^p \\ U_{pq0}^p \end{bmatrix}. \tag{7}$$

According to the small-signal model of the PLL [7], the phase difference caused by the injected perturbations can be obtained

$$\Delta\theta_1 = G_{\mathrm{PLL}} U^s_{pq}, \quad G_{\mathrm{PLL}} = \frac{K_{\mathrm{PLL}\_p} s + K_{\mathrm{PLL}\_i}}{s^2 + U^s_{d0} K_{\mathrm{PLL}\_p} s + U^s_{d0} K_{\mathrm{PLL}\_i}} \tag{8}$$

where $G_{\mathrm{PLL}}$ is the transfer function of the PLL, $K_{\mathrm{PLL}\_p}$ and $K_{\mathrm{PLL}\_i}$ represent the proportional gain and integral gain of the PLL controller, respectively. $U^s_{d0}$ is the $d$-axis steady-state value of the PCC voltage in the PCC-voltage $dq$-frame.

Since the steady-state values of the injected voltage perturbations $U^p_{pd,q0}$ in the perturbation-voltage $dq$-frame are zero, the dynamic influence of the PLL is avoided, as shown in (7). Therefore, the different bandwidths of PLL used for the perturbation injection have no effect on the accuracy of the impedance measurement.

On the other hand, the relationship between the current perturbation in the perturbation-voltage $dq$-frame and in the PCC-voltage $dq$-frame can be derived as

$$\begin{bmatrix} I^s_{pd} \\ I^s_{pq} \end{bmatrix} = \begin{bmatrix} \cos\theta_1 & \sin\theta_1 \\ -\sin\theta_1 & \cos\theta_1 \end{bmatrix} \begin{bmatrix} I^p_{pd} \\ I^p_{pq} \end{bmatrix}. \tag{9}$$

In addition, (7) can be simplified as

$$\begin{bmatrix} U^s_{pd} \\ U^s_{pq} \end{bmatrix} = \begin{bmatrix} \cos\theta_1 & \sin\theta_1 \\ -\sin\theta_1 & \cos\theta_1 \end{bmatrix} \begin{bmatrix} U^p_{pd} \\ U^p_{pq} \end{bmatrix} \tag{10}$$

where different values of $\theta_1$ represent different compositions of the current and voltage perturbations for the calculation of the impedance. This difference is equivalent to that caused by the perturbations injected at different electrical point of the system. Base on the impedance calculation algorithm given by (2), the voltage and current expression of (9) and (10), the measured impedance expressions $\mathbf{Y^m_{dq}}$ can be rewritten as

$$\mathbf{Y^m_{dq}} = \begin{bmatrix} \cos\theta_1 & \sin\theta_1 \\ -\sin\theta_1 & \cos\theta_1 \end{bmatrix} \mathbf{Y}^p_{\boldsymbol{dq}} \begin{bmatrix} \cos\theta_1 & \sin\theta_1 \\ -\sin\theta_1 & \cos\theta_1 \end{bmatrix}^{-1} = \mathbf{Y^s_{dq}} \tag{11}$$

where $\mathbf{Y}^s_{\boldsymbol{dq}}$ represents the admittance matrix of the converter in the PCC-voltage $dq$-frame (the desired admittance measurement).

From (11), it can be found that the initial phase of the perturbation injection has no influence on the impedance measurement, which means that the location of injecting perturbations into the system does not influence the impedance measurement results. This is because that the adopted impedance calculation algorithm is based on two groups of linearly independent equations, which have considered the coupling effect between the grid impedance and converter impedance. In contrast, in some other research works [22], [23] the impedance matrix is measured by dividing the converter impedance matrix into four SISO systems, where the influence of the initial phase angle on the perturbation injection is likely to bring about significant errors on the impedance measurement results.

## IV. Influence of Synchronization Dynamics on Impedance Calculation

Fig. 5 shows the PCC- and measured-voltage $dq$-frame when two linearly independent perturbations are injected into the system. Assuming the actual phase of the PCC voltage is $\theta$ and the estimated phase is $\theta_m$, there exists an angle difference between $\theta$ and $\theta_m$ due to the dynamic influence of the PLL used for the impedance calculation. Consequently, two angle differences, i.e., $\triangle\theta$ and $\triangle\theta'$, are generated. Therefore, the relationship between the measured voltage in the PCC-voltage $dq$-frame (superscript "$s$") and that in the PLL-estimated $dq$-frame (superscript "$m$") can be obtained, which are given by

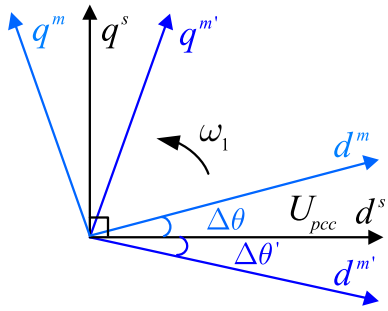


Fig. 5. PCC- and measured-voltage $dq$-frames.

$$\begin{bmatrix} U^m_{pd1} \\ U^m_{pq1} \end{bmatrix} = \begin{bmatrix} \cos(\Delta\theta) & \sin(\Delta\theta) \\ -\sin(\Delta\theta) & \cos(\Delta\theta) \end{bmatrix} \begin{bmatrix} U^s_{pd1} \\ U^s_{pq1} \end{bmatrix} \tag{12}$$

$$\begin{bmatrix} U^m_{pd2} \\ U^m_{pq2} \end{bmatrix} = \begin{bmatrix} \cos(\Delta\theta') & \sin(\Delta\theta') \\ -\sin(\Delta\theta') & \cos(\Delta\theta') \end{bmatrix} \begin{bmatrix} U^s_{pd2} \\ U^s_{pq2} \end{bmatrix}. \tag{13}$$

Based on (7) and (8), (12) and (13) can be combined as

$$\begin{bmatrix} U^m_{pd1} & U^m_{pd2} \\ U^m_{pq1} & U^m_{pq2} \end{bmatrix} = \begin{bmatrix} 1 & U^s_{q0} G_{\mathrm{PLL}} \\ 0 & 1 - U^s_{d0} G_{\mathrm{PLL}} \end{bmatrix} \begin{bmatrix} U^s_{pd1} & U^s_{pd2} \\ U^s_{pq1} & U^s_{pq2} \end{bmatrix} \tag{14}$$

where $U^s_{q0}$ denotes the $q$-axis steady-state value of the PCC voltage in the PCC-voltage $dq$-frame.

Similarly, the relationship between the current in the PCC-voltage $dq$-frame and that in the PLL-estimated $dq$-frame can be derived as

$$\begin{bmatrix} I^m_{pd1} & I^m_{pd2} \\ I^m_{pq1} & I^m_{pq2} \end{bmatrix} = \begin{bmatrix} I^s_{pd1} & I^s_{pd2} \\ I^s_{pq1} & I^s_{pq2} \end{bmatrix} + \begin{bmatrix} 0 & I^s_{q0} G_{\mathrm{PLL}} \\ 0 & -I^s_{d0} G_{\mathrm{PLL}} \end{bmatrix} \begin{bmatrix} U^s_{pd1} & U^s_{pd2} \\ U^s_{pq1} & U^s_{pq2} \end{bmatrix} \tag{15}$$

where $I^s_{d0,q0}$ denote the $d$-axis and $q$-axis steady-state value of the current in the PCC-voltage $dq$-frame, respectively.

According to (14) and (15), the relationship between the measured admittance $\mathbf{Y^m_{dq}}$ and the actual admittance$\mathbf{Y^s_{dq}}$ is derived as

$$\mathbf{Y^m_{dq}} = \left( \mathbf{Y^s_{dq}} + \begin{bmatrix} 0 & I^s_{q0} G_{PLL} \\ 0 & -I^s_{d0} G_{PLL} \end{bmatrix} \right) \cdot \begin{bmatrix} 1 & U^s_{q0} G_{\mathrm{PLL}} \\ 0 & 1 - U^s_{d0} G_{\mathrm{PLL}} \end{bmatrix}^{-1} \tag{16}$$

where a mismatch between the actual admittance and the measured admittance caused by the dynamic influence of the PLL can be clearly observed. Hence, in order to mitigate this effect on the admittance measurement results, the term $U^s_{d0} G_{\mathrm{PLL}}$ and $I^s_{d0} G_{\mathrm{PLL}}$ must be sufficiently small at the frequency of the interest. The terms $U^s_{d0} G_{\mathrm{PLL}}$ and $I^s_{d0} G_{\mathrm{PLL}}$ are equal to zero since in this case $I^s_{q0} = 0$, $U^s_{q0} = 0$.

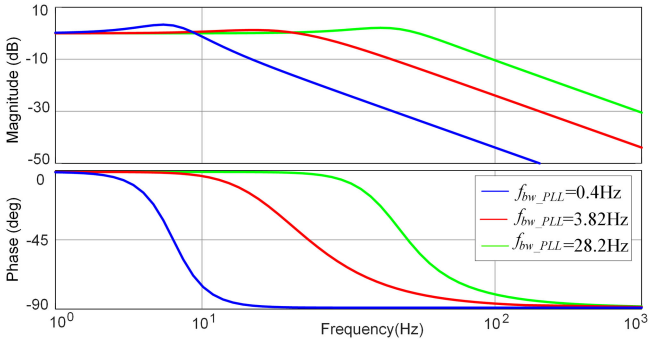


Fig. 6. Bode diagrams of the closed-loop transfer function of the PLL.

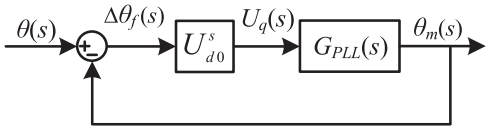


Fig. 7. Small-signal model of PLL.

Fig. 6 shows Bode plots of the closed loop transfer function of the PLL, i.e., $U^s_{d0}G_{\rm PLL}$. It is clear that the PLL behaves like a low-pass filter. When the bandwidth of the PLL is below the frequency of the injected perturbations, the perturbations can be filtered by the PLL, and consequently have little effect on the impedance measurement results. However, when the frequency of the injected perturbations is lower than the bandwidth of the PLL, those low-frequency components significantly influence the accuracy of the impedance measurement.

Since $I^s_{q0} < U^s_{d0}$ in general, the influence of the term $I^s_{d0}G_{\rm PLL}$ can also be ignored when the bandwidth of the PLL is lower than the lowest frequency of injected perturbations. Thus, in order to measure the impedance accurately, the bandwidth of the PLL is chosen to be much lower than the lowest injected perturbation frequency, which makes the measurement error negligible in the measured frequency range.

## V. Mitigation of Synchronization Dynamics for Impedance Measurement

This section first analyzes the influence of the system frequency variations on the accuracy of the phase estimation, and then an improved phase estimation method used for the impedance calculation is proposed.

### *A. Influence of the System Frequency Variations on the Phase Estimation*

Fig. 7 shows the small-signal model of the PLL, where $\triangle\theta_f$ is the angle difference between the PCC voltage angle $\theta$ and the estimated angle $\theta_m$. This phase difference is caused by the PLL when the system frequency variation exists, which is given by

$$\Delta\theta_f(s) = \frac{1}{1+U^s_{d0}G_{\rm PLL}(s)}\cdot\theta(s). \tag{17}$$

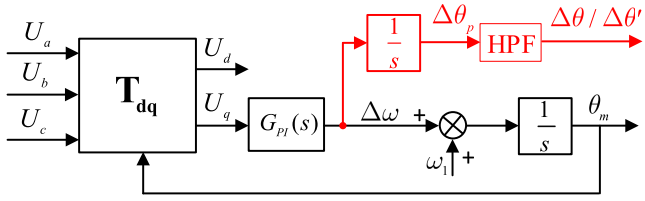


Fig. 8. Improved phase estimation method for the impedance calculation.

In the presence of the system frequency variation, the PCC voltage angle can be expressed by

$$\theta(t) = (\omega_1+\Delta\omega)t+\theta_0 = \omega_1 t + 2\pi K_{\rm ramp}t^2+\theta_0 \tag{18}$$

where $\omega_1$ is the fundamental frequency and $\theta_0$ is the initial phase. $K_{\rm ramp}$ is the ramp rate of frequency deviation [also refer to the rate of the frequency change (ROCOF)].

The PCC voltage angle can be expressed, in the frequency domain, as

$$\theta(s) = \frac{\omega_1}{s^2}+\frac{2\pi K_{\rm ramp}}{s^3} \tag{19}$$

According to the final theorem, the steady-state error $\triangle\theta_f$ can be defined as

$$\Delta\theta_f = \lim_{t\to\infty}e(t) = \lim_{s\to 0}s\Delta\theta_f(s) = \frac{2\pi K_{\rm ramp}}{U^s_{d0}K_{{\rm PLL}\_i}} \tag{20}$$

It is noted that the phase difference $\triangle\theta_f$ is related to the voltage magnitude, the ROCOF, and the integral gain of the PLL, which is determined by the PLL bandwidth. When the bandwidth of the PLL is too low to track the system frequency accurately as the system frequency varies, the phase difference $\triangle\theta_f = \triangle\omega t$ will become larger as time goes on. In this case, the measured voltage can be expressed by

$$\begin{bmatrix}U^m_{pd1}\\U^m_{pq1}\end{bmatrix} = \begin{bmatrix}\cos(\Delta\omega t) & \sin(\Delta\omega t)\\ -\sin(\Delta\omega t) & \cos(\Delta\omega t)\end{bmatrix}\begin{bmatrix}U^s_{pd1}\\U^s_{pq1}\end{bmatrix} \tag{21}$$

which indicates that the measured voltage is dependent on the system frequency variations and the measurement time.

Based on (20), the final angle difference $\triangle\theta_f$ can be small to reduce the error between the measured voltage and actual voltage, which means that the bandwidth of the PLL needs to be high. On the other hand, to reduce the dynamic influence of the PLL caused by the injected perturbations on the measured voltage and current, the bandwidth of PLL needs to be lower than the lowest injected perturbation frequency. There is, thus, a tradeoff in the design of the bandwidth of the PLL used with the impedance calculation.

### *B. Improved Phase Estimation Method for the Impedance Calculation*

Fig. 8 shows the basic block of the improved phase estimation method used for the impedance calculation. To track the system frequency variations, the bandwidth of the PLL need to be selected sufficiently high. Yet, the high bandwidth PLL introduces additional dynamic on the measured voltage and current. The relationship between the data in the measured- and in the

PCC-voltage *dq*-frame can be written as

$$\begin{bmatrix} U^s_{pd1} \\ U^s_{pq1} \end{bmatrix} = \begin{bmatrix} \cos(\Delta\theta) & \sin(\Delta\theta) \\ -\sin(\Delta\theta) & \cos(\Delta\theta) \end{bmatrix}^{-1} \begin{bmatrix} U^m_{pd1} \\ U^m_{pq1} \end{bmatrix} \quad (22)$$

$$\begin{bmatrix} I^s_{pd1} \\ I^s_{pq1} \end{bmatrix} = \begin{bmatrix} \cos(\Delta\theta) & \sin(\Delta\theta) \\ -\sin(\Delta\theta) & \cos(\Delta\theta) \end{bmatrix}^{-1} \begin{bmatrix} I^m_{pd1} \\ I^m_{pq1} \end{bmatrix}. \quad (23)$$

According to (22) and (23), the voltage and current in the PCC-voltage *dq*-frame (the desired *dq*-frame) can be acquired based on the voltage and current in the measured-voltage *dq*-frame as well as the extracted phase difference $\triangle\theta$. Consequently, the actual impedance of the converter can be obtained based on the corrected voltage and current.

To do the correction of the voltage and current, phase differences $\triangle\theta$ and $\triangle\theta'$ must be extracted accurately when injecting different perturbations. Since these phase differences are caused by the injection of the broadband excitation signals, they contain the corresponding frequency components of the perturbations. Considering both the filtering performance and the complexity of the filter design, a second-order high-pass filter is adopted to extract these phase differences composing of multiple frequencies components. The transfer function of the high-pass filter can be expressed as

$$G_{\mathrm{HPF}}(s) = \frac{s^2}{s^2 + 2\zeta\omega_n s + \omega_n^2} \quad (24)$$

where $\omega_n$ is the cutoff frequency of the filter and $\xi$ is the damping factor, which is generally chosen as 0.707.

It is noted that the selection of the cutoff frequency of the high-pass filter should be lower than the lowest frequency of the injected perturbations. This guarantees the extracted phase angle difference as accurate as possible.

## VI. Simulation Verification

In order to verify the theoretical analysis and the proposed estimation method for the synchronization phase angle, an impedance measurement setup shown in Fig. 3 is simulated. The PRBS is designed from 1.9 to 1000 Hz and its magnitude is chosen as 10% of the steady-state value of the current.

Table I shows the parameters of the converter under test. It is worth noting that the inherent dead time of the converter tends to modify the impedance model [24] and it is set as 2 $\mu$s in both the simulation model and hardware prototype. Since the admittance of $Y_{dd}$ and $Y_{qq}$ are much larger than the admittance of $Y_{dq}$ and $Y_{qd}$ when the power factor is high [7], only the measured results of $Y_{dd}$ and $Y_{qq}$ are provided in this paper for simplicity.

### A. Influence of the Synchronization Dynamics on Perturbation Injection

Table II shows four designed cases. Case 1 and Case 2 have different initial phases while Case 2 and Case 3 have different bandwidths of PLL that are used for the coordinate transformation of the perturbation injection. The frequency variations have been considered in Case 4.

Fig. 9 shows the admittance ($Y_{dd}$, $Y_{qq}$) of the converter under different angles used for the perturbation injection. It is noted

TABLE I
Parameters of the Converter Under Test

| Symbol | Description | Value |
|---|---|---|
| $K_{i\_p}/K_{i\_i}$ | Current inner controller | 6/1000 |
| $K_p/K_i$ | PI controller of PLL | 0.47/44.4 |
| $\omega$ | Grid frequency | 314 rad/s |
| $f_s$ | Sampling frequency | 10 *k*Hz |
| $I_{d0}$ | *d* channel current steady value | 8 A |
| $I_{q0}$ | *q* channel current steady value | 0 A |
| $U_{d0}$ | *d* channel voltage steady value | 400 V |
| $U_{q0}$ | *q* channel voltage steady value | 0 V |
| $U_{dc0}$ | DC voltage of converter | 730 V |
| $U_g$ | Grid phase-neutral peak voltage | 325 V |
| $L$ | Filtered inductor | 1.5 mH |
| $C_g$ | Grid capacitor | 15 $\mu$F |
| $T_d$ | Dead time | 2 $\mu$s |
| $L_g$ | Grid inductor | 7.5 mH |

TABLE II
Influence Factors for Perturbation Injection

| Case | ROCOF | PLL $K_{PLL\_p}/K_{PLL\_i}$ | Bandwidth | Initial Phase |
|---|---|---|---|---|
| Case 1 | 0.0 Hz/s | 0.47/44.4 | 28.2 Hz | 0° |
| Case 2 | 0.0 Hz/s | 0.47/44.4 | 28.2 Hz | 90° |
| Case 3 | 0.0 Hz/s | 0.03/0.20 | 2.0 Hz | 90° |
| Case 4 | 0.5 Hz/s | 0.47/44.4 | 28.2 Hz | 90° |

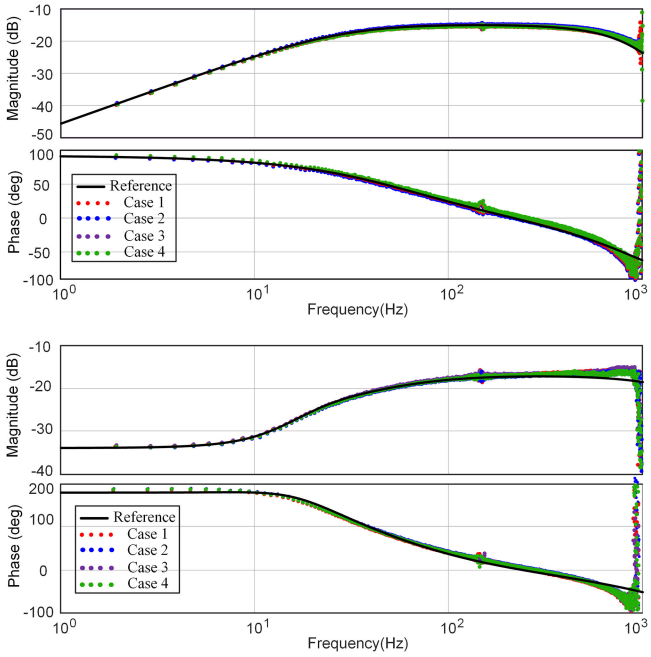


Fig. 9. Admittance of $Y_{dd}$ (top) and $Y_{qq}$ (below) under different synchronization angles for perturbation injection.

TABLE III
DIFFERENT BANDWIDTHS OF PLL

| Case | ROCOF | PLL $K_{PLL\_p}/K_{PLL\_i}$ | Bandwidth |
|---|---|---|---|
| Case 5 | 0.0 Hz/s | 0.01/0.04 | 0.4 Hz |
| Case 6 | 0.0 Hz/s | 0.03/0.20 | 2.0 Hz |
| Case 7 | 0.0 Hz/s | 0.47/4.44 | 9.5 Hz |
| Case 8 | 0.0 Hz/s | 0.47/44.4 | 28.2 Hz |

that four cases can obtain the same impedance measurement results, which means that the bandwidth of the PLL and the initial phase of the synchronization phase angle do not affect the measurement results. If the system frequency keeps changing, sufficiently high bandwidth of the PLL can guarantee the accuracy of the impedance measurement results and do not introduce the dynamic effects on the perturbation injection. Therefore, in order to track the system frequency variations accurately, the bandwidth of the PLL used for the generation of the synchronization phase for the perturbation injection can be selected as high as possible.

### *B. Influence of the Synchronization Dynamics on Impedance Calculation*

Table III designs four different cases considering different bandwidths of PLL used for impedance calculation. The bandwidth of PLL in Case 5 is much smaller than the lowest injected perturbation frequency (1.9 Hz) and Case 6 is approximate to the lowest perturbation frequency; while the bandwidths of PLL in Case 7 and Case 8 are larger than the lowest perturbation frequency.

Fig. 10 shows the admittance ($Y_{dd}$, $Y_{qq}$) of the converter under different bandwidths of PLL used for the impedance calculation. The bandwidth of PLL does not influence the measurement results of $Y_{dd}$; On the other hand, the bandwidth of PLL significantly influences the measured admittance of $Y_{qq}$.

The higher the bandwidth of PLL is, the larger the measured errors have. Since the bandwidth of the PLL is much smaller in Case 5, the impedance results in this case match with the analytical impedance model well. This is mainly because that the PLL used for the impedance calculation behaves like a low-pass filter, and the low bandwidth can help to reduce the influence of the injected perturbations on the output phase angle of the PLL. Therefore, in general, the bandwidth of the PLL for the impedance calculation is set much lower than the lowest injected perturbation frequency.

### *C. Influence of the Frequency Variations on Synchronization Phase for Impedance Calculation*

Table IV shows different ROCOFs and bandwidths of PLL. In Case 9 and Case 10, the ROCOF is so small that relatively low bandwidth of PLL can obtain good frequency tracking ability. In Case 11 and Case 12, the ROCOF is large, high bandwidth of the PLL is needed to track the frequency variations.

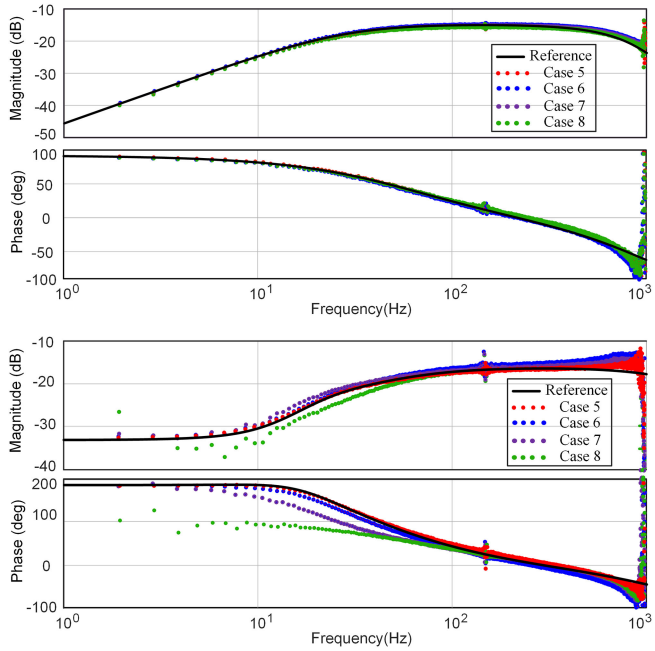


Fig. 10. Admittance of $Y_{dd}$ (top) and $Y_{qq}$ (below) under different bandwidths of PLL for impedance calculation.

TABLE IV
INFLUENCE OF FREQUENCY VARIATIONS

| Case | ROCOF | PLL $K_{PLL\_p}/K_{PLL\_i}$ | Bandwidth |
|---|---|---|---|
| Case 9 | 0.5 Hz/s | 0.01/0.04 | 0.4 Hz |
| Case 10 | 0.5 Hz/s | 0.10/1.0 | 4.4 Hz |
| Case 11 | 5.0 Hz/s | 0.10/1.0 | 4.4 Hz |
| Case 12 | 5.0 Hz/s | 0.47/44.4 | 28.2 Hz |

Fig. 11 shows different impedance measurement results considering the different rates of the frequency change and the different bandwidths of the PLL. The results show significant mismatch between the measured impedance and analytical impedance in Case 9 and Case 11. This is mainly because that the bandwidth of the PLL in Case 9 and Case 11 cannot track the frequency changes online so that the measured voltage and current are not synchronized with the actual *dq*-frame. By comparison, in Case 10 and Case 12, relatively accurate impedance measurement results can be obtained because the bandwidth of the PLL is sufficiently high, which is able to track the frequency variaitions to make the voltage and current synchronized.

Compared with the measurement results in Case 5, it is clear that there is a tradeoff between the selection of different bandwidths of PLL. Thus, when both the injected perturbations and system frequency variations exist, how to obtain the appropriate phase for the impedance calculation is the important issues.

### *D. Impedance Measurement Results Using Different Methods*

Table V shows three cases using different measurement methods, in which ROCOF is set as 0.5 Hz/s and the bandwidth of PLL is 28.2 Hz.

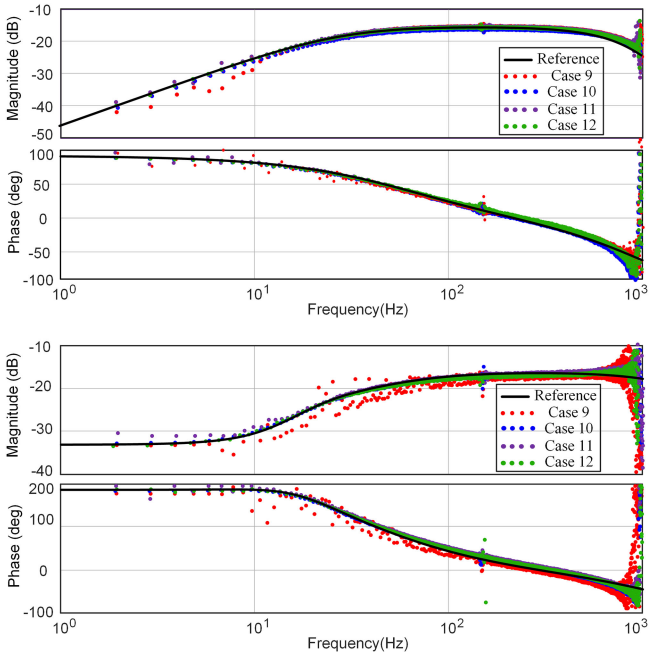


Fig. 11. Admittance of $Y_{dd}$ (top) and $Y_{qq}$ (below) under different ROCOFs and bandwidths of PLL for impedance calculation.

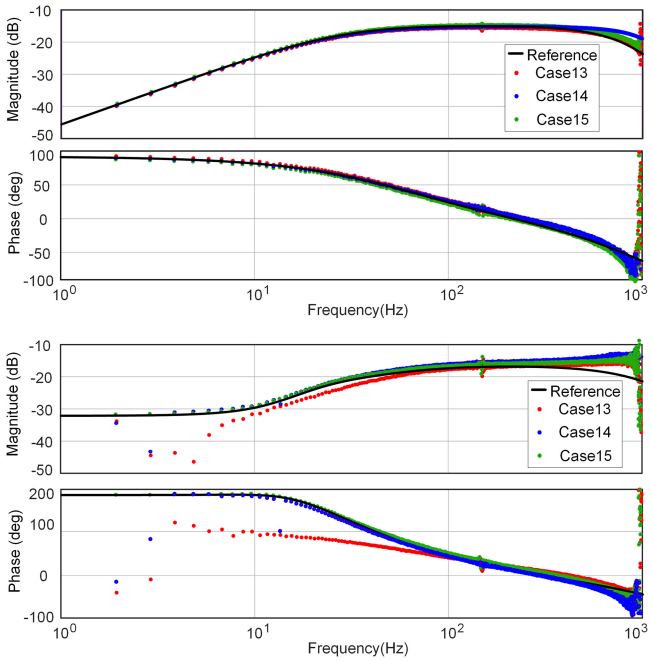


Fig. 12. Admittance of $Y_{dd}$ (top) and $Y_{qq}$ (below) based on different measurement methods.

TABLE V
DIFFERENT MEASUREMENT METHODS

| Case | ROCOF | PLL $K_{PLL\_p}/K_{PLL\_i}$ | Synchronization Phase Estimation |
|---|---|---|---|
| Case 13 | 0.5 Hz/s | 0.47/44.4 | Traditional PLL |
| Case 14 | 0.5 Hz/s | 0.47/44.4 | Proposed method in [15] |
| Case 15 | 0.5 Hz/s | 0.47/44.4 | Proposed method |

Fig. 12 shows the impedance measurement results using different measurement methods considering both the influence of the frequency variations and injected perturbations. It is seen from the Case 13 that the high-bandwidth PLL fails to extract an accurate synchronization phase, leading to significant errors in the impedance measurement results. However, the impedance measurement method proposed in [15] can obtain the accurate impedance results in large extent except for some frequency points that are below the bandwidth of the PLL used for the impedance calculation, which can be observed from Case 14. This is because that the correction matrix used in [15] is not invertible and cannot correct the measured data in these frequency points. In contrast, when adopting the method proposed in this paper, the measurement results based on this impedance calculation method can match with the analytical impedance model well.

## VII. EXPERIMENT VERIFICATION

Fig. 13 shows the detailed experimental setup of the impedance measurement unit. A programmable three-phase voltage source is used to emulate the power grid. Two Danfoss

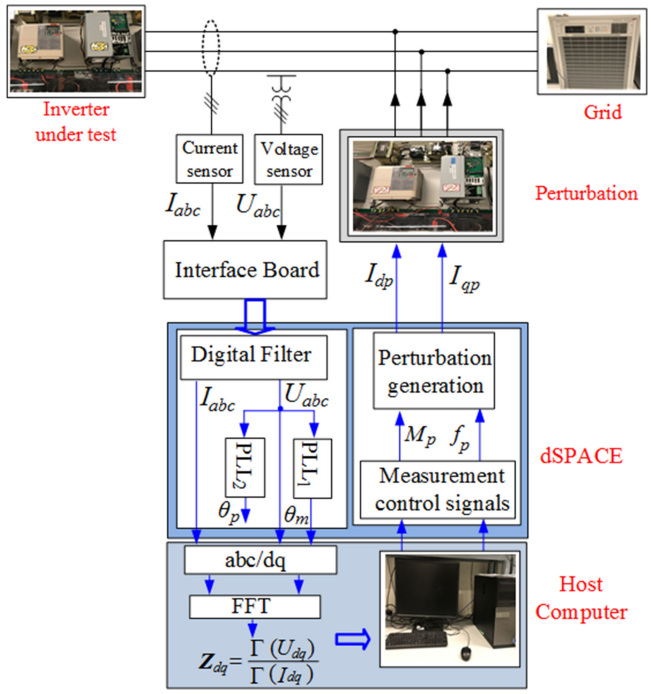


Fig. 13. Small-scale prototype of the impedance measurement system.

converters are used, one is considered as the inverter under test, the other is used as the source of the perturbation injection. The *dq*-domain output admittance of the converter is measured to validate the theoretical analysis on the impact of the synchronization phase angle used for impedance measurement. The current transducer LA 55-P and voltage transducer LV 25-P are used to acquire current and voltage signals for the calculation of the impedance. The sampled voltage and current are sent to

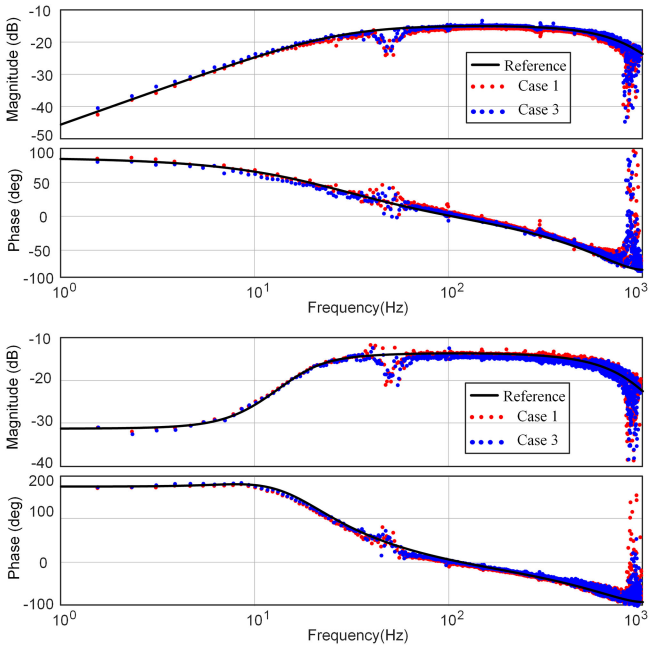


Fig. 14. Admittance of $Y_{dd}$ (top) and $Y_{qq}$ (below) under different synchronization angles for perturbation injection.

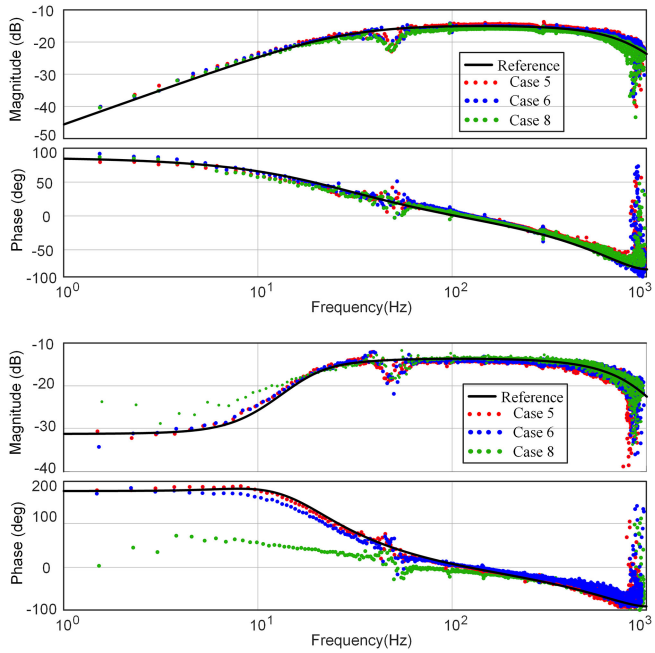


Fig. 15. Admittance of $Y_{dd}$ (top) and $Y_{qq}$ (below) under different bandwidths of PLL for impedance calculation.

the dSPACE and the synchronization phase is calculated based on the PLL and the voltage and current are recorded in the *dq*-domain.

In addition, the data are processed in the host computer and the impedances are calculated based on the impedance measurement algorithm. It is noted that all the measured admittance results appear spike around 50 Hz in the *dq*-frame. This is due to the existed background harmonic and does not affect the analysis results of the influence of the synchronization phase angle on perturbation injection and impedance calculation.

### *A. Influence of the Synchronization Dynamics on Perturbation Injection*

Fig. 14 shows the admittance of $Y_{dd}$ and $Y_{qq}$ under different synchronization angles used for the perturbation injection, in which Case 1 and Case 3 are chosen as the verified cases. Comparing with Fig. 9, the bandwidth of the PLL and the initial phase angle do not influence the impedance measurement results, which matches with the simulation results.

### *B. Influence of the Synchronization Dynamics on Impedance Calculation*

Fig. 15 shows the admittance of $Y_{dd}$ and $Y_{qq}$ under different synchronization angles for the impedance calculation, in which Case 5, Case 6, and Case 8 are chosen as the verified cases. Comparing with Fig. 10, the bandwidth of the PLL definitely influence the measured admittance of $Y_{qq}$ while the results of $Y_{dd}$ are not affected. Both the experiment and simulation results draw the same conclusion that lower bandwidth of the PLL is preferred to obtain accurate measurement results.

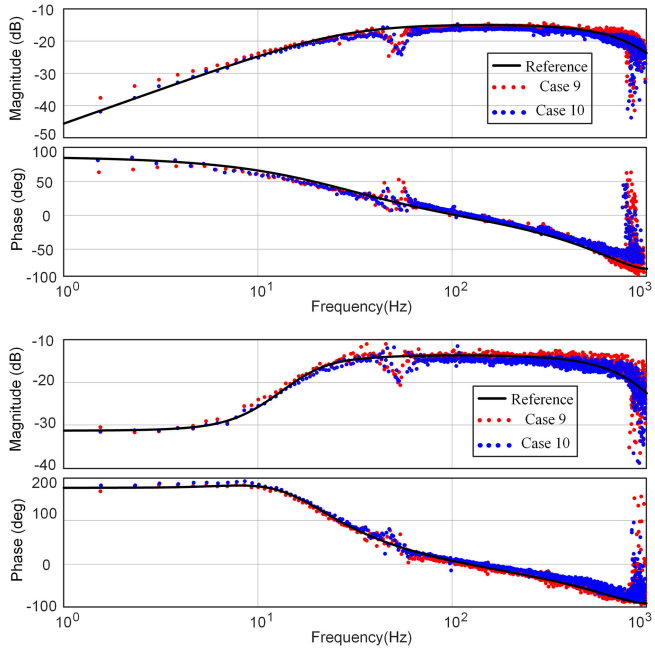


Fig. 16. Admittance of $Y_{dd}$ (top) and $Y_{qq}$ (below) under different bandwidths of PLL when the frequency varies.

### *C. Influence of the Frequency Variations on Synchronization Phase for Impedance Calculation*

Fig. 16 shows the measured admittance of $Y_{dd}$ and $Y_{qq}$ under different bandwidths of PLL when the system frequency varies. Since in the experiment the ROCOF (0.05 Hz/s) is smaller than the simulation, the measured error is relatively smaller. Nevertheless, the conclusion can be drawn that the low

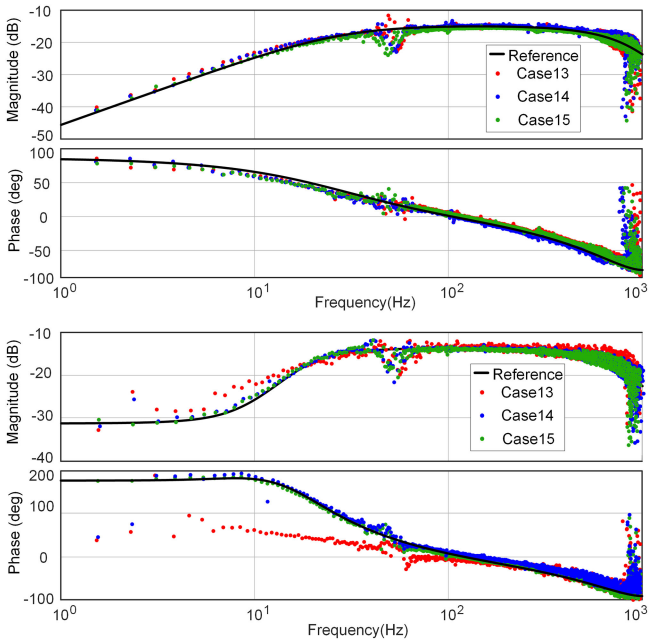


Fig. 17. Admittance of $Y_{dd}$ (top) and $Y_{qq}$ (below) based on different measurement methods.

bandwidth of the PLL cannot track the frequency variations, which causes the difference between the measured impedance and the analytical impedance especially in the low-frequency range.

### D. Impedance Measurement Results Using Different Methods

Fig. 17 shows the measured admittance results of $Y_{dd}$ and $Y_{qq}$ based on different measurement methods. It is noted that when both the injected perturbations and system frequency variations exist, the high bandwidth of the traditional PLL influences the measured results of $Y_{qq}$ significantly, as shown in Case 13. Nevertheless, when the measurement method proposed in [15] is adopted, the measured impedance results match the analytical impedance model in large extent, as shown in Case 14. On the other hand, the influence of the injected perturbations and the frequency variations on the impedance measurement results is eliminated when using the measurement method proposed in this paper.

## VIII. Conclusion

This paper has analyzed the influence of the synchronization phase on the definition of *dq*-frame used for the impedance measurement. The analysis has shown that the dynamics of the phase angle used for the impedance calculation have significant influences on the measurement results while the dynamics of the phase angle used for the perturbation injection have little impact on the impedance measurement. Based on the relationship between the voltage and current in the measured-voltage *dq*-frame and in the PCC-voltage *dq*-frame, an improved impedance calculation method is proposed, which can mitigate the influence of synchronization dynamics caused by both the injected perturbations and system frequency variations and, thus, can obtain the impedance accurately. The correctness of the theoretical analysis and the effectiveness of the proposed method have been confirmed by the simulations and experimental results.

## References

[1] F. Blaabjerg, Z. Chen, and S. B. Kjaer, "Power electronics as efficient interface in dispersed power generation systems," *IEEE Trans. Power Electron.*, vol. 19, no. 5, pp. 1184–1194, Sep. 2004.

[2] W. Cao, Y. Ma, L. Yang, F. Wang, and L. M. Tolbert, "D–Q impedance based stability analysis and parameter design of three-phase inverter-based AC power systems," *IEEE Trans. Ind. Electron.*, vol. 64, no. 7, pp. 6017–6028, Jul. 2017.

[3] B. Wen, D. Dong, D. Boroyevich, R. Burgos, P. Mattavelli and Z. Shen, "Impedance-based analysis of grid-synchronization stability for three-phase paralleled converters," *IEEE Trans. Power Electron.*, vol. 31, no. 1, pp. 26–38, Jan. 2016.

[4] X. Wang and F. Blaabjerg, "Harmonic stability in power electronic based power systems: concept, modeling, and analysis," *IEEE Trans. Smart Grid*, to be published, doi: 10.1109/TSG.2018.2812712.

[5] X. Wang, L. Harnefors, and F. Blaabjerg, "Unified impedance model of grid-connected voltage-source converters," *IEEE Trans. Power Electron.*, vol. 33, no. 2, pp. 1775–1787, Feb. 2018.

[6] S. Neshvad, S. Chatzinotas, and J. Sachau, "Wideband identification of power network parameters using pseudo-random binary sequences on power inverters," *IEEE Trans. Smart Grid*, vol. 6, no. 5, pp. 2293–2301, Sep. 2015.

[7] B. Wen, D. Boroyevich, R. Burgos, P. Mattavelli, and Z. Shen, "Small-signal stability analysis of three-phase AC systems in the presence of constant power loads based on measured d-q frame impedances," *IEEE Trans. Power Electron.*, vol. 30, no. 10, pp. 5952–5963, Oct. 2015.

[8] R. Burgos, D. Boroyevich, F. Wang, K. Karimi, and G. Francis, "On the AC stability of high power factor three-phase rectifiers," in *Proc. Energy Convers. Congr. Expo.*, Sep. 2010, pp. 2047–2054.

[9] Y. L. Familiant, K. A. Corzine, J. Huang, and M. Belkhayat, "AC impedance measurement techniques," in *Proc. IEEE Inter. Conf. Electric Mach. Drive.*, May 2005, pp. 1850–1857.

[10] A. Riccobono, M. Mirz, and A. Monti, "Noninvasive online parametric identification of three-phase AC power impedances to assess the stability of grid-tied power electronic inverters in LV networks," *IEEE J. Emerg. Sel. Topics Power Electron.*, vol. 6, no. 2, pp. 629–647, Jun. 2018.

[11] A. Riccobono, E. Liegmann, M. Pau, F. Ponci, and A. Monti, "Online parametric identification of power impedances to improve stability and accuracy of power hardware-in-the-loop simulations," *IEEE Trans. Instrum. Meas.*, vol. 66, no. 9, pp. 2247–2257, Sep. 2017.

[12] J. Huang, "AC/DC power system small-signal impedance measurement for stability analysis," Ph.D. dissertation, Dept. Elect. Eng., Missouri Univ. Sci. Technol., Rolla, MO, USA, 2009.

[13] T. Roinila, M. Vilkko, and J. Sun, "Online grid impedance measurement using discrete-interval binary sequence injection," *IEEE J. Emerg. Sel. Topics Power Electron.*, vol. 2, no. 4, pp. 985–993, Dec. 2014.

[14] T. Roinila *et al.*, "Hardware-in-the-loop methods for real-time frequency-response measurements of on-board power distribution systems," *IEEE Trans. Ind. Electron.*, to be published, doi: 10.1109/TIE.2018.2860543.

[15] Z. Shen, M. Jaksic, B. Zhou, P. Mattavelli, J. Verhulst, and M. Belkhayat, "Analysis of phase locked loop (PLL) influence on DQ impedance measurement in three-phase AC systems," in *Proc. Appl. Power Electron. Conf. Expo.*, Mar. 2013, pp. 939–945.

[16] J. H. Cho, K. Y. Choi, Y. W. Kim, and R. Y. Kim, "A novel P-Q variations method using a decoupled injection of reference currents for a precise estimation of grid impedance," in *Proc. Energy Convers. Congr. Expo.*, Sep. 2014, pp. 5059–5064.

[17] G. Francis, "An algorithm and system for measuring impedance in DQ coordinates," Ph.D. dissertation, Dept. Elect. Eng., Virginia Tech, Blacksburg, VA, USA, 2010.

[18] M. Cespedes and J. Sun, "Adaptive control of grid-connected inverters based on online grid impedance measurements," *IEEE Trans. Sustain. Energy*, vol. 5, no. 2, pp. 516–523, Apr. 2014.

[19] B. Miao, R. Zane, and D. Maksimovic, "System identification of power converters with digital control through cross-correlation methods," *IEEE Trans. Power Electron.*, vol. 20, no. 5, pp. 1093–1099, Sep. 2005.

[20] Z. Shen, "Online measurement of three-phase AC power system impedance in synchronous coordinates," Ph.D. dissertation, Dept. Elect. Eng., Virginia Tech, Blacksburg, VA, USA, 2012.

[21] J. Huang, K. A. Corzine, and M. Belkhayat, "Small-signal impedance measurement of power-electronics-based AC power systems using line-to-line current injection," *IEEE Trans. Power Electron.*, vol. 24, no. 2, pp. 445–455, Feb. 2009.
[22] T. Roinila, T. Messo, and E. Santi, "MIMO-identification techniques for rapid impedance-based stability assessment of three-phase systems in DQ domain," *IEEE Trans. Power Electron.*, vol. 33, no. 5, pp. 4015–4022, May 2018.
[23] T. Roinila and T. Messo, "Online grid-impedance measurement using Ternary-sequence injection," *IEEE Trans. Ind. Appl.*, vol. 54, no. 5, pp. 5097–5103, Sep. 2018.
[24] Z. Shen, M. Jaksic, S. Ahmed, P. Mattavelli and D. Boroyevich, "Parametric study of dead time effect on three phase AC output impedance of Voltage-source inverter (VSI)," in *Proc. Appl. Eu. Conf. Power Electron. Appl.*, Sep. 2011, pp. 1–8.

**Hong Gong** (S'18) was born in Sichuan, China, in 1992. He received both the B.S and M.S. degrees from Sichuan University, Chengdu, China, in 2014 and 2017, respectively. Since 2017, he has been working toward the Ph.D. degree at the Aalborg University, Aalborg, Denmark.

His research interests include modeling and control of grid-connected converters, impedance measurement.

**Dongsheng Yang** (S'13–M'17) was born in Jiangsu Province, China, in 1984. He received the B.S., M.S., and Ph.D. degrees in electrical engineering from the Nanjing University of Aeronautics and Astronautics, Nanjing, China, in 2008, 2011, and 2016, respectively.

Since 2016, he has been with Aalborg University, Aalborg, Denmark, where he is currently an assistant professor in the Department of Energy, Aalborg University, Aalborg, Denmark. His main research interests include design and control of grid-connected inverters, harmonic analysis and mitigation in power-electronic-based power systems, and online impedance measurement techniques.

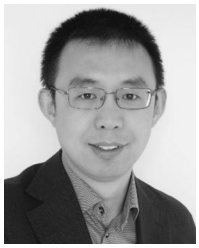

**Xiongfei Wang** (S'10–M'13–SM'17) received the B.S. degree from Yanshan University, Qinhuangdao, China, in 2006, the M.S. degree from the Harbin Institute of Technology, Harbin, China, in 2008, both in electrical engineering, and the Ph.D. degree in energy technology from Aalborg University, Aalborg, Denmark, in 2013.

Since 2009, he has been with the Department of Energy Technology, Aalborg University, where he is currently a Professor and Research Program Leader for Electronic Grid Infrastructure. His research interests include modeling and control of grid-interactive power converters, harmonics analysis and control, passive and active filters, stability of power electronic based power systems.

Dr. Wang is an Associate Editor for the IEEE TRANSACTIONS ON POWER ELECTRONICS, the IEEE TRANSACTIONS ON INDUSTRY APPLICATIONS, and the IEEE JOURNAL OF EMERGING AND SELECTED TOPICS IN POWER ELECTRONICS. In 2016, he was selected for Aalborg University Strategic Talent Management Program for the next-generation research leaders. He received four IEEE prize paper awards, the outstanding reviewer award of IEEE TRANSACTIONS ON POWER ELECTRONICS in 2017, and the IEEE PELS Richard M. Bass Outstanding Young Power Electronics Engineer Award in 2018.